Acta Geochim (2023) 42:988–997
https://doi.org/10.1007/s11631-023-00632-8

ORIGINAL ARTICLE

Thermal expansivity of geikielite and ilmenite utilizing in-situ synchrotron X-ray diffraction at high temperature

Jiamei Song[1,2] · Dawei Fan[1] · Shijie Huang[1,2] · Shanrong Zhang[1,2] · Mengzeng Wu[1,2] · Wei Chen[1,2,3] · Wenge Zhou[1]

Received: 31 March 2023 / Revised: 12 July 2023 / Accepted: 24 July 2023 / Published online: 19 August 2023

Abstract The unit-cell parameters and volumes of geikielite ($MgTiO_3$) and ilmenite ($FeTiO_3$) were investigated at high temperatures up to 700 K and ambient pressure, using in-situ angle-dispersive synchrotron X-ray diffraction. No phase transition was detected over the experimental temperature range. Using (Berman in J Petrol 29:445–522, 1988. 10.1093/petrology/29.2.445) equations to fit the temperature-volume data, the volumetric thermal expansion coefficients at ambient conditions (α_{V0}) of $MgTiO_3$ and $FeTiO_3$ were obtained as follows: 2.55 (6) × 10^{-5} K^{-1} and 2.82 (10) × 10^{-5} K^{-1}, respectively. We infer that the larger effective ionic radius of Fe^{2+}(VI) (0.78 Å) than that of Mg^{2+}(VI) (0.72 Å) renders $FeTiO_3$ has a larger volumetric thermal expansivity than $MgTiO_3$. Simultaneously, the refined axial thermal expansion coefficients under ambient conditions are α_{a0} = 0.74 (3) × 10^{-5} K^{-1} and α_{c0} = 1.08 (5) × 10^{-5} K^{-1} for the *a*-axis and *c*-axis of $MgTiO_3$, respectively, and α_{a0} = 0.95 (5) × 10^{-5} K^{-1} and α_{c0} = 0.92 (12) × 10^{-5} K^{-1} for the *a*-axis and *c*-axis of $FeTiO_3$, respectively. The axial thermal expansivity of $MgTiO_3$ is anisotropic, but that of $FeTiO_3$ is nearly isotropic. We infer that the main reason for the different axial thermal expansivity between $MgTiO_3$ and $FeTiO_3$ is that the thermal expansion mode of the Mg-O bond in $MgTiO_3$ is different from that of the Fe–O bonds in $FeTiO_3$.

Keywords Geikielite · Ilmenite · Thermal expansion · Synchrotron X-ray diffraction · High temperature

1 Introduction

The lunar interior is thought to consist of various mineral accumulations resulting from the crystallization differentiation of early magmatic oceans (Wieczorek et al. 2006). At the end stage of the early lunar evolution, the ilmenite-bearing cumulates (IBCs) layer, which is composed mainly of ilmenite ($FeTiO_3$), is formed in the upper lunar mantle, and then overturned and sunk to the deep lower lunar mantle (Zhao et al. 2019). The downwelling of IBCs after lunar mantle overturning has an important impact on the dynamics and thermal evolution of the lunar mantle (Xu 2010). The density characteristics of IBCs, especially the density of $FeTiO_3$ at the corresponding pressure and temperature conditions, are one of the key parameters to gain insight into the dynamics process of lunar mantle overturning (Li et al. 2019).

The density characteristics of $FeTiO_3$ require the thermodynamic parameters of $FeTiO_3$ under the corresponding high pressure and temperature conditions. Among them, the thermal expansion coefficient is an important thermodynamic parameter for constructing the density model of $FeTiO_3$ under the corresponding high pressure and temperature conditions. Thus, the study of the thermal expansion coefficient of $FeTiO_3$ is fundamental for constructing the density model of lunar mantle under the

✉ Dawei Fan
fandawei@vip.gyig.ac.cn

[1] Key Laboratory of High-Temperature and High-Pressure Study of the Earth's Interior, Institute of Geochemistry, Chinese Academy of Sciences, Guiyang 550081, Guizhou, China

[2] University of Chinese Academy of Sciences, Beijing 100049, China

[3] Guizhou Polytechnic of Construction, Guiyang 551400, Guizhou, China

corresponding high pressure and temperature conditions, and then understanding the density characteristics of IBCs and the dynamic process of the lunar mantle overturning.

Previous studies have shown that $FeTiO_3$ and geikielite ($MgTiO_3$) can form unlimited solid solution (Lindsley 1991; Linton et al. 1999) along with crystallization and differentiation of lunar magmatic ocean. In addition, according to the existing detailed mineral composition analysis of Apollo samples, Luna samples, and lunar meteorites, the lunar ilmenite always contains a certain percentage of geikielite. Specifically, the typical content of geikielite in the lunar ilmenite sample is $\sim$ 5 vol%, and the maximum is up to $\sim$ 33 vol% (Alexander et al. 2014, 2016; Anand et al. 2003; Donohue and Neal 2018; Heiken et al. 1991; Hu 2015; Joy et al. 2008; Klemme et al. 2006; Shearer et al. 1991; Snape et al. 2014).

Both $FeTiO_3$ and $MgTiO_3$ are ABO_3-type oxides, which belong to the trigonal system with space group *R* (Fig. 1). Mg^{2+} can completely replace Fe^{2+} at the A cation of $FeTiO_3$ to form $MgTiO_3$. In addition, both $FeTiO_3$ and $MgTiO_3$ consist of AO_6 (A = Mg, Fe), BO_6 (B = Ti), and VO_6 (vacancy, which means lacking central ion). A and B cations occupy two-thirds of the octahedral sites in an orderly manner, and AO_6 and BO_6 octahedrons have an equal number of divalent (A^{2+}) and tetravalent (B^{4+}) cations, forming alternate layers along the hexagon *c* direction, and one-third of the octahedral sites are vacant. XO_6 (X = A, B) forms a hexagonal ring centered on VO_6 and extends within the same layer, and then the AO_6 and BO_6 layers are interleaved alternately. The ratio of AO_6, BO_6, and VO_6 is 1:1:1 within the same layer. Along the *a*-axis, a pair of shared side BO_6 octahedrons is separated by

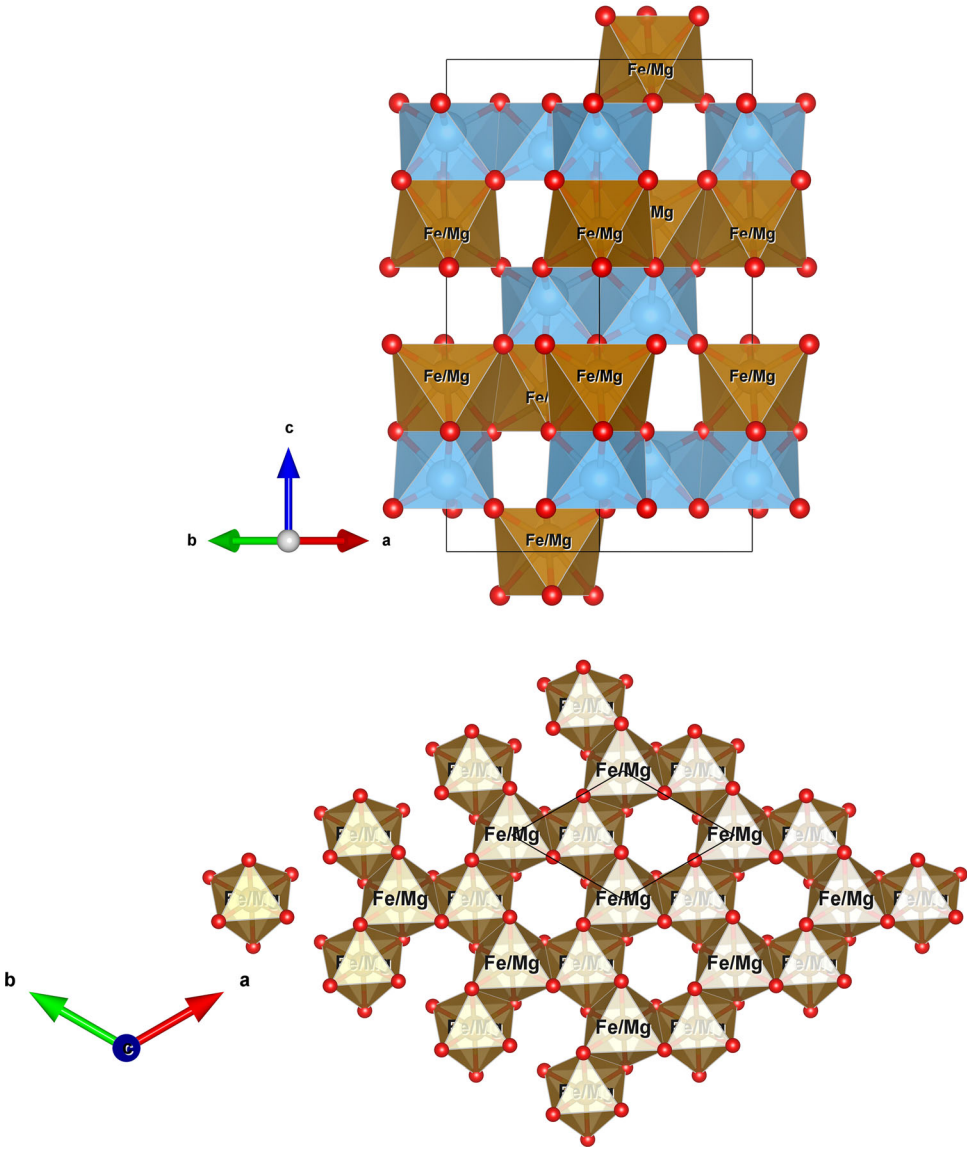

Fig. 1 Crystal structure (vertical and side views) of $FeTiO_3$ and $MgTiO_3$ at ambient conditions ($R\bar{3}$). The crystal structure data are obtained from Yamanaka et al. (2005, 2007)

cationic vacancies and diagonally by an AO_6 octahedron. Along the *c*-axis, the cells are arranged in the order of AO_6–BO_6–VO_6–BO_6–AO_6–VO_6.

To date, only a few previous studies conducted the thermal expansion behavior of $FeTiO_3$ and $MgTiO_3$ at high temperatures using various experimental methods. For $FeTiO_3$, Wechsler and Prewitt (1984) first researched the high-temperature thermal expansion behavior of $FeTiO_3$ from 297 to 1323 K using the conventional single-crystal X-ray diffraction method. Hereafter, Harrison et al. (2000) studied the thermal expansivity of $FeTiO_3$ from 293 to 1598 K using the in-situ neutron powder diffraction method. However, there was a significant difference in the thermal expansion coefficients between Wechsler and Prewitt (1984) and Harrison et al. (2000). For $MgTiO_3$, Henderson et al. (2009) first investigated the thermal expansivity of $MgTiO_3$ at high temperatures from 296 to 1305 K using in-situ neutron powder diffraction method. Subsequently, Tuval et al. (2020) also measured the thermal expansivity of $MgTiO_3$ from 298 to 1163 K using the conventional powder X-ray diffraction method. However, both the experimental samples of Henderson et al. (2009) and Tuval et al. (2020) contain non-negligible impurities, and there is also a big difference in the calculated thermal expansion coefficients between Henderson et al. (2009) and Tuval et al. (2020). Therefore, there are still many deficiencies at present in understanding the thermal expansion behavior of $FeTiO_3$ and $MgTiO_3$, and further systematic studies are needed.

In this study, we investigated the thermal expansion behaviors of $MgTiO_3$ and $FeTiO_3$ at high temperatures up to 700 K by in-situ synchrotron radiation X-ray diffraction (XRD) combined with diamond anvil cell (DAC). Moreover, the potential influencing factors on the volumetric thermal expansivity of $MgTiO_3$ and $FeTiO_3$ and the different axial thermal expansivities between $MgTiO_3$ and $FeTiO_3$ were further discussed.

2 Samples and analytical methods

The $MgTiO_3$ and $FeTiO_3$ samples in this study are high-purity (> 99%) powders procured by Aladdin Corporation. The samples were heated for two hours at a constant temperature of 100 °C in a furnace to remove the absorbed moisture and then examined via conventional powder XRD using an Empyrean X-ray diffractometer (DY1411). The cermet X-ray tube (Cu target) has a maximum powder wavelength of 1.5406 Å, a voltage of 40 kV, an operating current of 40 mA, and a range of 5.0051-70°. The ambient XRD spectra of $MgTiO_3$ and $FeTiO_3$ were indexed based on the standard spectra JCPDS 79-0831 and JCPDS 75-1203, respectively, confirming that the crystal structures of $MgTiO_3$ and $FeTiO_3$ are trigonal and belong to the *R* space group.

High temperature and ambient pressure experiments were carried out by using a modified Merrill-Bassett type DAC (Fan et al. 2010, 2014) mounted with two pairs of 400 μm culet-sized diamond anvils. For the $MgTiO_3$ sample, a gasket made of rhenium tablet was preindented to ~ 54 μm thick, and then a ~ 220 μm hole was drilled as the sample chamber. Similarly, for the $FeTiO_3$ sample, a gasket made from T301 stainless steel was pre-indented to a thickness of ~ 75 μm and then drilled to a diameter of ~ 230 μm, serving as the sample chamber. The $FeTiO_3$ and $MgTiO_3$ sample powders were slightly pressed between two opposing diamond anvils to form an approximately 50 μm thick disk, and a piece of $FeTiO_3$ or $MgTiO_3$ sample about 200 μm in diameter was loaded into the sample chamber. The high temperature was generated by an external resistance heating device made up of a 0.3 mm diametric NiCr resistor wire. Using a $Pt_{90}Rh_{10}$-Pt_{100} thermocouple adhered to a diamond anvil pavilion, the accuracy of measuring the experimental temperature is ± 1 K. The temperature was increased from room temperature to the maximum temperature of 700 K with an interval of 50 K, while the heating was kept for 300 s before the collection of the powder diffraction spectrum. In addition, the typical exposure time for collecting diffraction patterns of the sample is 300 s. Additional details about the experimental device and DAC components can be found in Fan et al. (2010).

In-situ high-temperature synchrotron radiation angle-dispersive XRD (ADXRD) experiments were conducted at the 4W2 beam-line of the Beijing Synchrotron Radiation Facility (BSRF). The wavelength of the monochromatic X-ray beam is 0.6199 Å calibrated by scanning through the Mo metal *K*-absorption edge. Diffraction patterns were amassed using the Pilatus detector. The X-ray beam was collimated to a beam dimension of 20 × 30 μm^2 through a pair of Kirkpatrick-Baez mirrors. CeO_2 powder was used as the standard for XRD to calibrate the tilting and rotation of the detector to the incident X-ray beam. The sample-detector distance was calculated from the powder CeO_2 diffraction pattern at ambient conditions.

All collected diffraction patterns were integrated in terms of 2θ using the Fit2D program to obtain conventional one-dimensional profiles (Hammersley et al. 1996). The unit-cell parameters and volumes were calculated according to the 11 and 14 diffraction peaks identified from the XRD patterns of $MgTiO_3$ and $FeTiO_3$, respectively (Fig. 2). Then the diffraction peak positions were fitted using the OriginPro 8.5 software, and the unit-cell parameters and volumes were calculated using UnitCell software (Holland and Redfern 1997). Finally, the

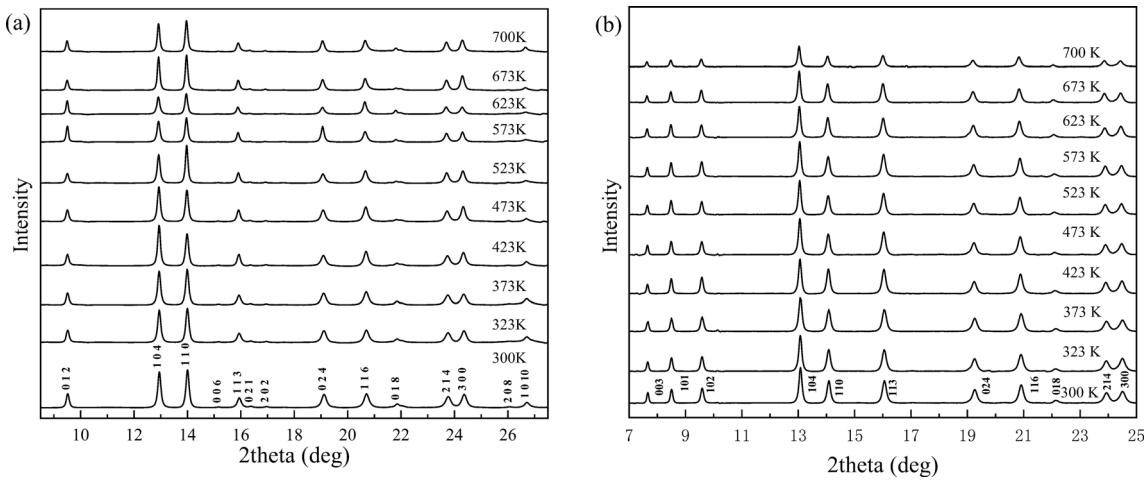

Fig. 2 Representative X-ray diffraction patterns of $FeTiO_3$ (**a**) and $MgTiO_3$ (**b**) obtained in this study up to 700 K at ambient pressure

volumetric and axial thermal expansion coefficients were fitted using *EoSFit* 7 software (Angel et al. 2014).

3 Results

The ambient XRD images of $MgTiO_3$ and $FeTiO_3$ in this study were also obtained at the 4W2 beam-line of BSRF, and the unit-cell parameters and volumes at ambient conditions are shown as follows: $a_0 = 5.0592(7)$ Å, $c_0 = 13.889(3)$ Å, and $V_0 = 307.87(8)$ Å^3 for $MgTiO_3$ and $a_0 = 5.0871(7)$ Å, $c_0 = 14.070(5)$ Å, and $V_0 = 315.33(10)$ Å^3 for $FeTiO_3$. Since the ionic radius of Mg^{2+} is smaller than that of Fe^{2+}, the formed Mg^{2+}-O bond is shorter than the Fe^{2+}-O bond (Henderson et al. 2009; Liferovich and Mitchell 2006; Wechsler and Prewitt 1984; Wechsler and Von Dreele 1989; Yamanaka et al. 2005), and all of the unit-cell parameters and volumes of the $MgTiO_3$ sample at ambient conditions are smaller than those of the $FeTiO_3$ sample.

The evolution of the XRD patterns of $MgTiO_3$ and $FeTiO_3$ in the experimental temperature range are shown in Fig. 2, where all peaks shift toward lower 2θ angles as the temperatures increase from 300 to 700 K at ambient pressure. The characteristic of the XRD patterns of $MgTiO_3$ and $FeTiO_3$ samples is that the narrow peaks are independent of each other (Fig. 2), which means that the data have high reliability. No peaks disappeared or new peaks appeared within the experimental temperature range, indicating that both $MgTiO_3$ and $FeTiO_3$ are stable within the experimental temperature conditions in this study. The unit-cell parameters and volumes of $MgTiO_3$ and $FeTiO_3$ at various temperature conditions are listed in Tables 1 and 2, respectively. Moreover, when the experimental temperature reaches 673 K, the unit-cell parameters and volume of $FeTiO_3$ suddenly decrease. However, previous studies

Table 1 Unit-cell parameters in $MgTiO_3$ at high temperature and ambient pressure

T (K)	a (Å)	c (Å)	V (Å^3)	c/a
300	5.0592 (7)	13.889 (3)	307.87 (8)	2.7453
323	5.0601(7)	13.895 (3)	308.11 (8)	2.7460
373	5.0620 (7)	13.899 (3)	308.43 (8)	2.7458
423	5.0636 (7)	13.906 (3)	308.79 (8)	2.7463
473	5.0654 (7)	13.916 (3)	309.24 (8)	2.7473
523	5.0674 (7)	13.922 (3)	309.59 (8)	2.7474
573	5.0690 (7)	13.931 (3)	309.99 (8)	2.7483
623	5.0714 (7)	13.938 (3)	310.44 (8)	2.7484
673	5.0732 (7)	13.945 (3)	310.82 (8)	2.7488
700	5.0740 (7)	13.949 (3)	311.01 (8)	2.7491

Numbers in parenthesis represent standard deviations

Table 2 Unit-cell parameters in $FeTiO_3$ at high temperature and ambient pressure

T (K)	a (Å)	c (Å)	V (Å^3)	c/a
300	5.0871 (7)	14.070 (5)	315.33 (10)	2.76582
323	5.0885 (7)	14.074 (5)	315.60 (10)	2.76584
373	5.0908 (7)	14.078 (5)	315.97 (10)	2.76538
423	5.0933 (7)	14.082 (5)	316.37 (10)	2.76481
473	5.0953 (8)	14.091 (5)	316.82 (10)	2.76549
523	5.0979 (8)	14.098 (5)	317.31 (10)	2.76545
573	5.1005 (8)	14.105 (5)	317.78 (10)	2.76542
623	5.1028 (8)	14.112 (5)	318.23 (10)	2.76554
673	5.1006 (8)	14.099 (5)	317.64 (10)	2.76418
700	5.1012 (8)	14.097 (5)	317.69 (10)	2.76347

Numbers in parenthesis represent standard deviations

(Wechsler and Prewitt 1984; Harrison et al. 2000) have not shown the same phenomenon at higher temperatures. We consider that the main reason for this difference is that the previous high-temperature measurements were carried out under the conditions of controlling the oxygen fugacity of the sample chamber. Such as, Wechsler and Prewitt (1984) studied only one quadrant of reciprocal space to minimize the total exposure of sample chamber at high temperatures. In addition, Harrison et al. (2000) even used a more stringent means of anti-oxidation, i.e. $FeTiO_3$ was placed in a vacuum furnace for high temperature experiments. Thus, we infer that the oxidation (or partial oxidation) of Fe^{2+} (0.780 Å) to Fe^{3+} (0.645 Å) in $FeTiO_3$ caused the sudden drop of the unit-cell parameters and volumes of $FeTiO_3$ at 673 K. Certainly, further experiments (e.g. recovering the experimental samples for Mössbauer spectroscopy measurement) are needed to confirm whether Fe^{2+} oxidation occurs at 673 K.

The temperature-volume (*T*-*V*) statistics (Tables 1 and 2, Fig. 3) were used to fit the volumetric thermal expansion coefficients of $MgTiO_3$ and $FeTiO_3$ at temperatures up to 700 K and 623 K, respectively. In this study, the high-temperature data are fitted with the thermal expansion expression proposed by Berman (1988), and the formula is as follows:

$$V_T = V_0 \times (1 + \alpha_0 \times (T - T_{ref}) + \frac{1}{2} \times \alpha_1 \times (T - T_{ref})^2) \quad (1)$$

where V_T is the unit-cell volume at elevated temperatures and ambient pressure, V_0 represents the unit-cell volume under ambient conditions, and T_{ref} is the reference temperature. The relationship between the thermal expansion coefficient and temperature is expressed by the parameters α_0 and α_1 as follows: $\alpha \approx [\alpha_0 + \alpha_1(T - T_{ref})]$. The parameter α_0 is the thermal expansion coefficient at T_{ref}. Figure 3 shows the volumetric thermal expansivities of $MgTiO_3$ and $FeTiO_3$ as a function of the temperature in this study. For comparison, the results of Henderson et al. (2009), Tuval et al. (2020), Wechsler and Prewitt (1984), and Harrison et al. (2000) are also plotted on these figures. By fitting the Eq. (1) based on the unit-cell volumes in this study with the *EoSFit* 7 program, we obtained the volumetric thermal expansion coefficients at ambient conditions $\alpha_{V0} = 2.55\ (6) \times 10^{-5}\ K^{-1}$ for $MgTiO_3$ and $\alpha_{V0} = 2.82\ (10) \times 10^{-5}\ K^{-1}$ for $FeTiO_3$ (Two data points with temperatures above 623 K were not used for fitting).

Figures 4 and 5 show the axial thermal expansivities of $MgTiO_3$ and $FeTiO_3$ as a function of temperature. By fitting the unit-cell parameter data (*a* and *c*) of $MgTiO_3$ and $FeTiO_3$ at high temperatures up to 700 K and 623 K using a "linearized" Berman's equation $l_T = l_0 \times (1 + \alpha_0 \times (T - T_{ref}))$ ($l = a, b, c$) with the *EoSFit* 7 program (Angel et al. 2014; Gonzalez-Platas et al. 2016), the refined unit-cell parameters at ambient conditions were obtained as follows: $a_0 = 5.0591(4)$ Å and $c_0 = 13.889(2)$ Å for $MgTiO_3$ and $a_0 = 5.0871(4)$ Å and $c_0 = 14.069(3)$ Å for $FeTiO_3$. The refined unit-cell parameters at ambient conditions are consistent with the measured results at ambient conditions in this study within their uncertainties (Tables 1 and 2). Simultaneously, the refined axial thermal expansion coefficients under ambient conditions are $\alpha_{a0} = 0.74\ (3) \times 10^{-5}\ K^{-1}$ and $\alpha_{c0} = 1.08\ (5) \times 10^{-5}\ K^{-1}$ for $MgTiO_3$ and $\alpha_{a0} = 0.95\ (5) \times 10^{-5}\ K^{-1}$ and $\alpha_{c0} = 0.92\ (12) \times 10^{-5}\ K^{-1}$ for $FeTiO_3$ (Two data points with temperatures above 623 K were not used for fitting).

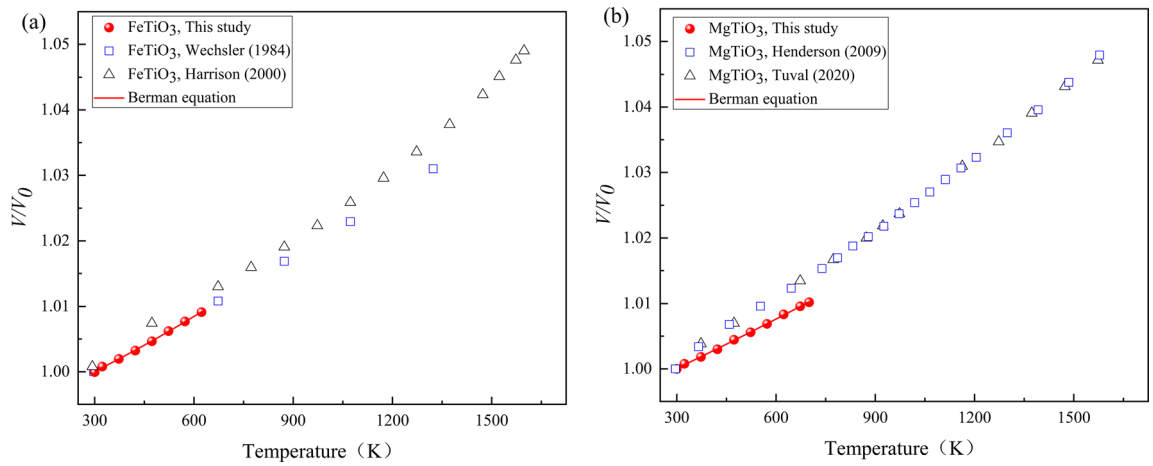

Fig. 3 *T*–*V* data of $FeTiO_3$ (**a**) and $MgTiO_3$ (**b**) at ambient pressure ((Harrison et al. 2000; Henderson et al. 2009; Tuval et al. 2020; Wechsler and Prewitt 1984). The error bars for the data points are not displayed because they are smaller than the symbols

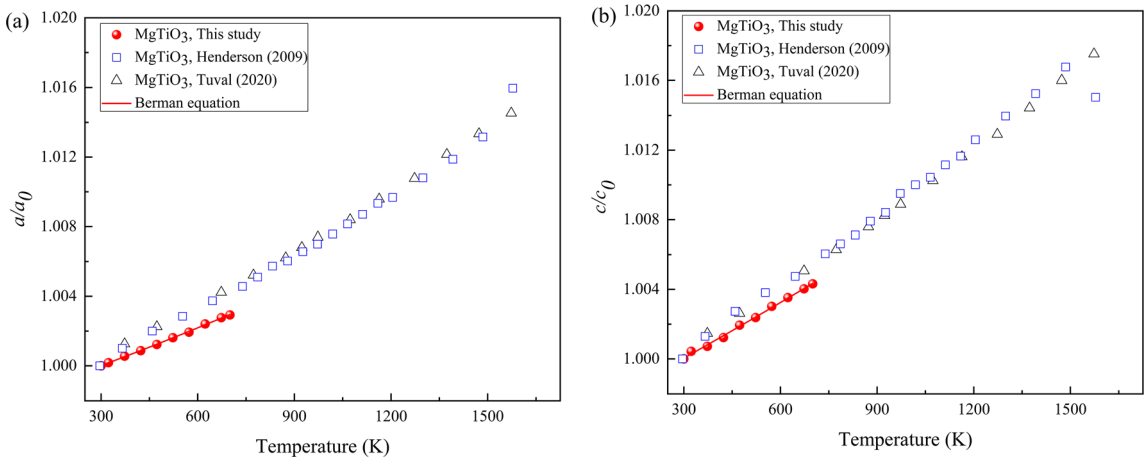

Fig. 4 Temperature dependence of the unit-cell parameters a and c of $MgTiO_3$ at room pressure (Henderson et al. 2009; Tuval et al. 2020)

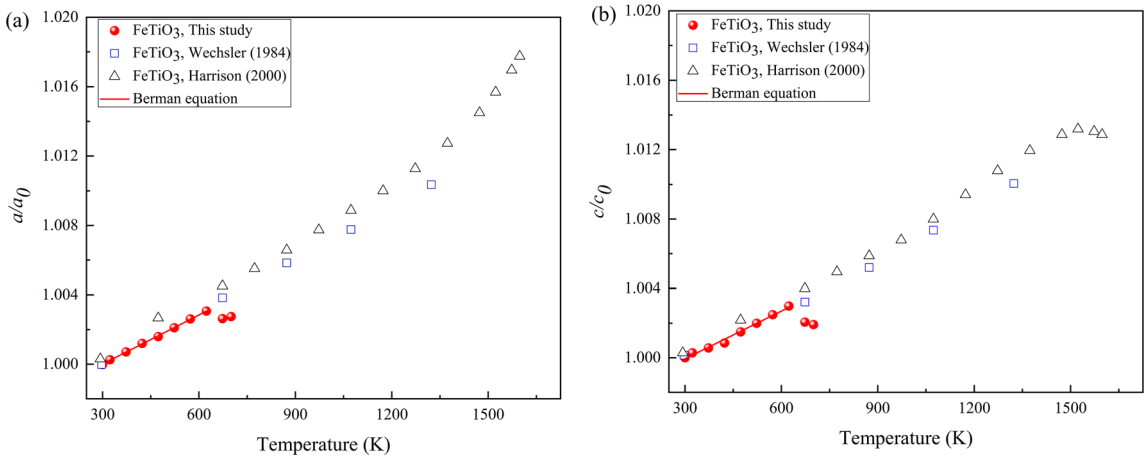

Fig. 5 Temperature dependence of the unit-cell parameters a and c of $FeTiO_3$ at room pressure (Harrison et al. 2000; Wechsler and Prewitt 1984)

4 Discussion

The thermal expansion coefficients of $MgTiO_3$ and $FeTiO_3$ have been investigated by some previous studies. Table 3 shows a detailed comparison between the thermal expansion coefficients of $FeTiO_3$ and $MgTiO_3$ obtained in this study and previous studies.

For $FeTiO_3$, only Wechsler and Prewitt (1984) and Harrison et al. (2000) investigated the temperature dependence of the unit-cell parameters and volumes of $FeTiO_3$ at high temperatures, but they have not given the volumetric and axial thermal expansion coefficients of $FeTiO_3$. Thus, we recalculated the volumetric and axial thermal expansion coefficients of $FeTiO_3$ by fitting their unit-cell parameters and volumes of $FeTiO_3$ at high temperatures using Berman's equation (Berman 1988), and the results are shown in Table 3 and Fig. 5 (Two data points with temperatures above 1500 K were not used for fitting). From Table 3, we can find that the values of volumetric thermal expansion coefficient of $FeTiO_3$ at ambient conditions from this study and previous studies are within the range of (2.82–3.62) $\times$ 10^{-5} K^{-1}. In this study, the obtained α_{V0} = 2.82 (10) $\times$ 10^{-5} K^{-1} for $FeTiO_3$ is roughly similar to the α_{V0} = 3.02 (4) $\times$ 10^{-5} K^{-1} obtained by Wechsler and Prewitt (1984) within their uncertainties. However, both of them are $\sim$ 17%–22% lower than the α_{V0} = 3.62 (10) $\times$ 10^{-5} K^{-1} obtained by Harrison et al. (2000). However, the exact reasons for the reported α_{V0} of Harrison et al. (2000) larger than those of this study and Wechsler and Prewitt (1984) are still unknown.

For $MgTiO_3$, Henderson et al. (2009) and Tuval et al. (2020) investigated the thermal expansion behavior of $MgTiO_3$ at high temperatures. For the convenience of comparison, their thermal expansion coefficients were obtained by fitting the Berman equation (Table 3). From Table 3, we can find that the values of volumetric thermal expansion coefficient of $MgTiO_3$ at ambient conditions from this study and previous studies are within the range of

Table 3 The refined unit-cell parameters and volumes, and thermal expansion coefficients of $MgTiO_3$ and $FeTiO_3$ at ambient conditions by using Berman's equations

	l_0(Å^3)/V (Å^3)	Alpha ($\times 10^{-5}$ K^{-1})	References
$MgTiO_3$			
a	5.0591 (4)	0.74 (3)	
c	13.889 (2)	1.08 (5)	This study
V	307.85 (5)	2.55 (6)	
a	5.0557 (4)	0.94 (3)	
c	13.901 (2)	1.25 (5)	Henderson et al. (2009)
V	307.69 (7)	3.12 (9)	
a	5.0535 (2)	0.845 (5)	
c	13.902 (1)	1.094 (6)	Tuval et al. (2020)
V	307.46 (3)	2.78 (1)	
$FeTiO_3$			
a	5.0871 (4)	0.95 (5)	
c	14.069 (3)	0.92 (12)	This study
V	315.31 (6)	2.82 (10)	
a	5.0885 (2)	1.02 (1)	
c	14.083 (3)	0.96 (3)	Wechsler and Prewitt (1984)
V	315.76 (8)	3.02 (4)	
a	5.0865 (17)	1.23 (5)	
c	14.088 (2)	1.05 (2)	Harrison et al. (2000)
V	315.56 (28)	3.62 (10)	

Numbers in parenthesis represent standard deviations

(2.55–3.12) $\times 10^{-5}$ K^{-1}. The obtained $\alpha_{V0} = 2.55$ (6) $\times 10^{-5}$ K^{-1} for $MgTiO_3$ in this study is $\sim$ 8% and $\sim$ 18% lower than the $\alpha_{V0} = 2.78$ (1) $\times 10^{-5}$ K^{-1} and 3.12 (9) $\times 10^{-5}$ K^{-1} obtained by Tuval et al. (2020) and Henderson et al. (2009), respectively. By carefully observing the composition characteristics of $MgTiO_3$ samples from Tuval et al. (2020) and Henderson et al. (2009), we can find that their $MgTiO_3$ samples are impure and contain a certain amount of impurities. For example, the $MgTiO_3$ sample used in Tuval et al. (2020) contains $\sim$ 5% Mg_2TiO_4 (qandilite), and the experimental sample used in Henderson et al. (2009) is $MgTi_2O_5$ which is the mixture of geikielite ($MgTiO_3$) and rutile (TiO_2). When samples have other impurity phases, the XRD peaks of samples may overlap with the diffraction signal of the impurity component, which will affect the accuracy of refined unit-cell parameters and volumes of samples. Thus, we infer that the impurities in the $MgTiO_3$ samples of previous studies may affect their volumetric thermal expansion coefficients of $MgTiO_3$.

In summary, the thermal expansion coefficients reported in this study are more reliable compared to those reported in previous studies because of the higher accuracy of the synchrotron XRD method and the higher purity of the samples of $FeTiO_3$ and $MgTiO_3$ used in this study. Furthermore, this study also has more experimental points in the temperature range of 300–700 K, and $FeTiO_3$ and $MgTiO_3$ samples were studied under the same experimental system to effectively avoid systematic errors between different experimental systems. All of the above-mentioned factors will result in smaller errors and higher accuracy of unit-cell parameters and volumes, and then obtain more reliable thermal expansion coefficients. Therefore, the influence of components of $FeTiO_3$ and $MgTiO_3$ on their volumetric and axial thermal expansion coefficients will be discussed next based on the obtained results in this study.

From Table 3, we can find that the obtained α_{V0} of $FeTiO_3$ in this study is $\sim$ 10.6% larger than that of $MgTiO_3$ in this study. As we know, both the Mg and Fe ions occupy the A site in the $MgTiO_3$ and $FeTiO_3$, and the crystal structure difference between $MgTiO_3$ and $FeTiO_3$ mainly lies in the change of metal cation types at the A site. The effective ionic radius of Fe^{2+}(VI) (0.78 Å) is larger than that of Mg^{2+}(VI) (0.72 Å) (Shannon 1976) at A site, which results in that the average bond length of Fe^{2+}–O (2.1406 Å) in $FeTiO_3$ (Yamanaka et al. 2007) is larger than that of Mg^{2+}-O (2.10785 Å) in $MgTiO_3$ (Culbertson et al. 2020). Therefore, the bond strengths of Fe^{2+}-O at A site in $FeTiO_3$ are weaker than that of the Mg^{2+}-O at A site in $MgTiO_3$ due to the larger bond length; accordingly, $FeTiO_3$ has larger volumetric thermal expansivity than $MgTiO_3$.

$MgTiO_3$ in this study shows the thermal expansion behavior of the *c*-axis direction is larger than that of the *a*-axis direction. This indicates that $MgTiO_3$ is anisotropic axial thermal expansivity (Fig. 6). However, $FeTiO_3$ in this study shows the thermal expansion behavior of the *c*-axis direction is close to that of the *a*-axis direction. This indicates that $FeTiO_3$ is quasi-isotropic axial thermal expansivity (Fig. 6). What causes such huge differences in the axial thermal expansion behaviors between $FeTiO_3$ and $MgTiO_3$? Next, we will try to discuss the possible reasons.

From the crystal structure of ilmenite-type minerals, ilmenite has a honeycomb structure along the *ab* plane and alternating layers along the *c* direction (Fig. 1). The thermal expansion along the *ab* plane at high temperatures is determined by the mutual constraint in each plane, and the thermal expansion along *c* direction is the average of each layer based on mutual superposition. Moreover, the thermal expansion along the *ab* plane and *c* direction are mutually constrained. For $MgTiO_3$, the cells tend to expand more along the *c*-axis than the *a*-axis because the interlayer forces are small, and it is difficult to elongate or bend the Mg–O, Ti–O bond within the layer.

However, $FeTiO_3$ is different from $MgTiO_3$. When $FeTiO_3$ is heated to expand under high temperatures, the variation of the Ti–Ti bond length across the vacancy is approximately linear with the unit-cell volume. In contrast, the Fe–Fe bonds across vacancies are shortened rather than elongated when heated (Wechsler and Prewitt 1984). This anomaly implies that the essential cause of the anomalous thermal expansion of $FeTiO_3$ is the Fe ion. The Fe–O bonds in $FeTiO_3$ can be divided into longer and shorter ones; the shorter Fe–O bond is more difficult to elongate along its axes but easier to bend, and the elongation of the longer Fe–O bond is twice that of the shorter one with the increase of temperature (Zhang et al. 2017). Analyzing the effect of the FeO_6 layer and TiO_6 layer on the thermal expansion separately for $FeTiO_3$, it can be seen that in $FeTiO_3$, the thermal expansion along the *c*-axis is smaller than that along the *a*-axis for the FeO_6 layer, while the opposite is true for the TiO_6 layer. Thus, we infer that the combined influences of FeO_6 and TiO_6 layers in $FeTiO_3$ ultimately lead to its isotropic axial thermal expansivity. In addition, there are non-negligible magnetic properties between the FeO_6 layers in $FeTiO_3$ that weakly affect its thermal expansion behavior (Sanson et al. 2014).

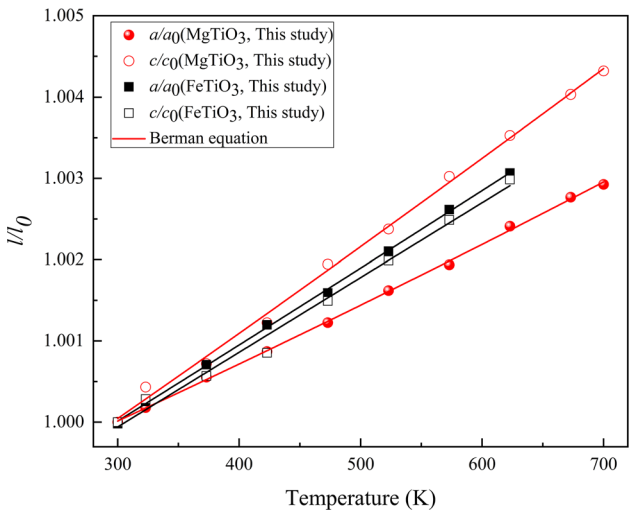

Fig. 6 The axial expansion of $MgTiO_3$ and $FeTiO_3$ as a function of temperature. The error bars for the data points are not displayed because they are smaller than the symbols

Fe is the transition metal element but Mg is not, thus FeO_6 in the $FeTiO_3$ is suitable for Ligand Field Theory (Dagroot et al. 1990) due to the d-layer electrons of transition metals, while MgO_6 in the $MgTiO_3$ is not applicable. Therefore, FeO_6 has different deformation mechanisms from MgO_6 when heated. A metal–metal interaction is allowed between the d orbitals extending their lobes through the face shared by the two octahedra, so the d orbital plane of Fe will extend its lobe through the shared surface of FeO_6 (Chen et al. 2013). This allows the transfer of valence electrons along the Fe–O–Ti path, which makes the Fe^{2+}/Ti^{4+} part become a Fe^{3+}/Ti^{3+} structure. As a result, the structure of $FeTiO_3$ is closer to the corundum structure (Radtke et al. 2006), which weakens the anisotropy of axial thermal expansibility and makes it closer to isotropic thermal expansivity. The intrinsic anharmonicity or electronic defects significantly affect the heat capacity and thermal expansion of $FeTiO_3$. In summary, the specificities of Fe ions and their relative bonds in $FeTiO_3$ are the main reasons for the obvious difference in the axial thermal expansivity between $FeTiO_3$ and $MgTiO_3$.

In this study, we obtained the thermal expansion coefficients of $FeTiO_3$ and $MgTiO_3$. The thermal expansion coefficient is one of the essential thermal equations of state parameters to build the density model of $FeTiO_3$ and $MgTiO_3$ under the corresponding conditions of the lunar mantle. However, besides the thermal expansion coefficient, there still needs more thermal equations of state parameters, such as the bulk modulus and its pressure and temperature derivatives, which are jointly applied to the construction of the lunar mantle density model. In the future, we still need to carry out further research about the bulk modulus and its pressure and temperature derivatives of $FeTiO_3$ and $MgTiO_3$, and then we can discuss the density models of $FeTiO_3$ and $MgTiO_3$, the density model of lunar mantle and the kinetic process of lunar mantle overturning.

5 Conclusion

(1) In-situ high temperature experiments of $MgTiO_3$ and $FeTiO_3$ were conducted by synchrotron radiation ADXRD and DAC. No phase changes were observed for $MgTiO_3$ and $FeTiO_3$ within the temperature range (300–700 K).

(2) By using Berman's equation to fit *T*–*V* data, $\alpha_{V0} = 2.55\ (6) \times 10^{-5}\ K^{-1}$ and $\alpha_{V0} = 2.82\ (10) \times 10^{-5}\ K^{-1}$ of $MgTiO_3$ and $FeTiO_3$ are obtained. Meanwhile, we also obtained the axial thermal expansion coefficients for $MgTiO_3$ and $FeTiO_3$ along the *a*-axis ($\alpha_{a0} = 0.74\ (3) \times 10^{-5}\ K^{-1}$ and $\alpha_{a0} = 0.95\ (5) \times 10^{-5}\ K^{-1}$, respectively) and *c*-axis ($\alpha_{c0} = 1.08\ (5) \times 10^{-5}\ K^{-1}$ and $\alpha_{c0} = 0.92\ (12) \times 10^{-5}\ K^{-1}$, respectively).

(3) The possible reasons for the difference between the volumetric thermal expansion coefficients of $FeTiO_3$ and $MgTiO_3$ are discussed. It is found that different compositions (Fe and Mg) at A site affect their volumetric thermal expansion coefficients.

(4) The potential factors influencing the axial thermal expansion coefficients of $MgTiO_3$ and $FeTiO_3$ and the possible reasons for the different axial thermal expansion anisotropy between $MgTiO_3$ and $FeTiO_3$ were discussed. We infer that the specificity of Fe ions in $FeTiO_3$ may be the main reason for the difference in the axial thermal expansivity between $FeTiO_3$ and $MgTiO_3$.

Acknowledgements This project was supported by National Natural Science Foundation of China (U2032118 and 42172048), Guizhou Provincial Science and Technology Projects (QKHPTRC-YQK[2023]035 and QKHJC-ZK[2021]ZD042), Hundred Talents Program of the Chinese Academy of Sciences, and Guizhou Provincial 2020 and 2021 Science and Technology Subsidies (Nos. GZ2020SIG and GZ2021SIG). The high-temperature XRD experiments were conducted at the 4W2 of the Beijing Synchrotron Radiation Facility (BSRF).

Author contributions JS Methodology, Data analysis, Investigation, Writing-original draft, Writing-review & editing, Visualization. DF Supervision, Conceptualization, Review & editing. Shijie Huang: Methodology, Investigation. SZ Methodology, Investigation. MW Methodology, Investigation. WC Methodology, Investigation. WZ Investigation, Review & editing.

Data availability Data will be made available on request.

Declarations

Competing interest The authors declare that they have no known competing financial interests or personal relationships that could have appeared to influence the work reported in this paper.

References

Alexander L, Snape JF, Crawford IA, Joy KH, Downes H (2014) Searching for nonlocal lithologies in the Apollo 12 regolith: a geochemical and petrological study of basaltic coarse fines from the Apollo lunar soil sample 12023,155. Meteorit Planet Sci 49:1288–1304. https://doi.org/10.1111/maps.12319

Alexander L, Snape JF, Joy KH, Downes H, Crawford IA (2016) An analysis of Apollo lunar soil samples 12070, 889, 12030, 187, and 12070, 891: Basaltic diversity at the Apollo 12 landing site and implications for classification of small-sized lunar samples. Meteorit Planet Sci 51:1654–1677. https://doi.org/10.1111/maps.12689

Anand M, Taylor LA, Neal CR, Snyder GA, Patchen A, Sano Y, Terada K (2003) Petrogenesis of lunar meteorite EET 96008. Geochim et Cosmochim Acta 67:3499–3518. https://doi.org/10.1016/S0016-7037(03)00134-0

Angel RJ, Alvaro M, Gonzalez-Platas J (2014) EosFit7c and a Fortran module (library) for equation of state calculations. Zeitschrift für Kristallographie-Crystalline Materials 229:405–419. https://doi.org/10.1515/zkri-2013-1711

Berman RG (1988) Internally-consistent thermodynamic data for minerals in the system Na_2O–K_2O–CaO–MgO–FeO–Fe_2O_3–Al_2O_3–SiO_2–TiO_2–H_2O–CO_2. J Petrol 29:445–522. https://doi.org/10.1093/petrology/29.2.445

Chen S, Huang M, Lin P, Jeng H, Lee J, Haw S, Chen S, Lin H, Lu K, Chen D, Dou S, Wang X, Chen J (2013) Orbital structure of $FeTiO_3$ ilmenite investigated with polarization-dependent X-ray absorption spectroscopy and band structure calculations. Appl Phys Lett 102:042107. https://doi.org/10.1063/1.4789992

Culbertson CM, Flak AT, Yatskin M, Cheong PH-Y, Cann DP, Dolgos MR (2020) Neutron total scattering studies of group ii titanates ($ATiO_3$, A^{2+}= Mg, Ca, Sr, Ba). Sci Rep 10:3729. https://doi.org/10.1038/s41598-020-60475-8

Degroot F, Grioni M, Fuggle JC, Thole B, Ghijsen J, Sawatzky G (1990) Ligand field effects in xas of 3d-transition metal compounds. In: Conference proceedings 25

Donohue PH, Neal CR (2018) Textural and mineral chemical evidence for the cumulate origin and evolution of high-titanium basalt fragment 71597. Am Mineral: J Earth Planet Mater 103:284–297. https://doi.org/10.2138/am-2018-6173

Fan D, Xu J, Liu J, Li Y, Xie H (2014) Thermal equation of state of natural stibnite up to 25.7 GPa and 533 K. High Temp High Pressures 43:351–359

Fan D, Zhou W, Wei S, Liu Y, Ma M, Xie H (2010) A simple external resistance heating diamond anvil cell and its application for synchrotron radiation X-ray diffraction. Rev Sci Instr 81:053903. https://doi.org/10.1063/1.3430069

Gonzalez-Platas J, Alvaro M, Nestola F, Angel R (2016) EosFit7-GUI: a new graphical user interface for equation of state calculations, analyses and teaching. J Appl Crystallogr 49:1377–1382. https://doi.org/10.1107/S1600576716008050

Hammersley AP, Svensson O, Hanfland M, Fitch AN, Hausermann DM (1996) Two-dimensional detector software: from real detector to idealised image or two-theta scan. Int J High Pressure Res 14:235–248. https://doi.org/10.1080/08957959608201408

Harrison RJ, Redfern SAT, Smith RI (2000) In-situ study of the R 3 to R 3 c phase transition in the ilmenite-hematite solid solution using time-of-flight neutron powder diffraction. Am Miner 85:194–205. https://doi.org/10.2138/am-2000-0119

Heiken GH, Vaniman DT, French BM (1991) Lunar Sourcebook, a user's guide to the Moon. Cambridge University Press

Henderson CMB, Neuhoff KS, Lennie AR (2009) Temperature dependence of rutile (TiO_2) and geikielite ($MgTiO_3$) structures

determined using neutron powder diffraction. Open Mineral J 3:1–11. https://doi.org/10.2174/1874456700903010001
Holland TJB, Redfern SAT (1997) Unit cell refinement from powder diffraction data: the use of regression diagnostics. Mineral Mag 61:65–77. https://doi.org/10.1180/minmag.1997.061.404.07
Hu Z (2015) Moon: origin and evolution. Science Press
Joy KH, Crawford IA, Anand M, Greenwood RC, Franchi IA, Russell SS (2008) The petrology and geochemistry of Miller Range 05035: a new lunar gabbroic meteorite. Geochim et Cosmochim Acta 72:3822–3844. https://doi.org/10.1016/j.gca.2008.04.032
Klemme S, Günther D, Hametner K, Prowatke S, Zack T (2006) The partitioning of trace elements between ilmenite, ulvospinel, armalcolite and silicate melts with implications for the early differentiation of the moon. Chem Geol 234:251–263. https://doi.org/10.1016/j.chemgeo.2006.05.005
Li H, Zhang N, Liang Y, Wu B, Dygert NJ, Huang J, Parmentier EM (2019) Lunar cumulate mantle overturn: a model constrained by ilmenite rheology. J Geophys Res: Planets 124:1357–1378. https://doi.org/10.1029/2018JE005905
Liferovich RP, Mitchell RH (2006) The pyrophanite–geikielite solid-solution series: crystal structures of the $Mn_{1-x}Mg_xTiO_3$ series ($0<x<0.7$). Can Mineral 44:1099–1107. https://doi.org/10.2113/gscanmin.44.5.1099
Lindsley DH (1991) Oxide minerals: petrologic and magnetic significance. Rev Mineral Geochem
Linton JA, Fei Y, Navrotsky A (1999) The $MgTiO_3$–$FeTiO_3$ join at high pressure and temperature. Am Miner 84:1595–1603. https://doi.org/10.2138/am-1999-1013
Radtke G, Lazar S, Botton GA (2006) High-resolution EELS investigation of the electronic structure of ilmenites. Phys Rev B Condensed Matter Mater Phys 74:155117. https://doi.org/10.1103/PhysRevB.74.155117
Sanson A, Mathon O, Pascarelli S (2014) Local vibrational dynamics of hematite (alpha-Fe_2O_3) studied by extended x-ray absorption fine structure and molecular dynamics. J Chem Phys 140:224504. https://doi.org/10.1063/1.4882282
Shannon RD (1976) Revised effective ionic radii and systematic studies of interatomic distances in halides and chalcogenides. Acta Crystallogr Sect a: Cryst Phys Diffract Theor Gen Crystallogr 32:751–767. https://doi.org/10.1107/S0567739476001551
Shearer CK, Papike JJ, Galbreath KC, Shimizu N (1991) Exploring the lunar mantle with secondary ion mass spectrometry: a comparison of lunar picritic glass-beads from the apollo-14 and apollo-17 sites. Earth Planet Sci Lett 102:134–147. https://doi.org/10.1016/0012-821X(91)90003-Z
Snape JF, Joy KH, Crawford IA, Alexander L (2014) Basaltic diversity at the Apollo 12 landing site: inferences from petrologic examinations of the soil sample 12003. Meteorit Planet Sci 49:842–871. https://doi.org/10.1111/maps.12285
Tuval T, Rosen BA, Zabicky J, Kimmel G, Dilman H, Shneck RZ (2020) Thermal expansion of $MgTiO_3$ made by sol-gel technique at temperature range 25–890 °C. Crystals 10:887. https://doi.org/10.3390/cryst10100887
Wechsler BA, Prewitt CT (1984) Crystal structure of ilmenite ($FeTiO_3$) at high temperature and at high pressure. Am Miner 69:176–185
Wechsler BA, Von Dreele RB (1989) Structure refinements of Mg_2TiO_4, $MgTiO_3$ and $MgTi_2O_5$ by time-of-flight neutron powder diffraction. Acta Crystallogr B 45:542–549. https://doi.org/10.1107/S010876818900786X
Wieczorek MA, Jolliff BL, Khan A, Pritchard ME, Weiss BP, Williams JG, Hood LL, Righter K, Neal CR, Shearer CK (2006) The constitution and structure of the lunar interior. Rev Mineral Geochem 60:221–364. https://doi.org/10.2138/rmg.2006.60.3
Xu Y (2010) Mare basalts and lunar evolution. Geochimica 39:50–62. https://doi.org/10.19700/j.0379-1726.2010.01.008
Yamanaka T, Komatsu Y, Nomori H (2007) Electron density distribution of $FeTiO_3$ ilmenite under high pressure analyzed by MEM using single crystal diffraction intensities. Phys Chem Miner 34:307–318. https://doi.org/10.1007/s00269-007-0149-7
Yamanaka T, Komatsu Y, Sugahara M, Nagai T (2005) Structure change of $MgSiO_3$, $MgGeO_3$, and $MgTiO_3$ ilmenites under compression. Am Miner 90:1301–1307. https://doi.org/10.2138/am.2005.1621
Zhang N, Wang H, Wang G (2017) In-situ high temperature X-ray diffraction study of hematite. Acta Petrologica Et Mineralogica 36:89–95. https://doi.org/10.3969/j.issn.1000-6524.2017.01.008
Zhao Y, de Vries J, van den Berg AP, Jacobs MHG, van Westrenen W (2019) The participation of ilmenite-bearing cumulates in lunar mantle overturn. Earth Planet Sci Lett 511:1–11. https://doi.org/10.1016/j.epsl.2019.01.022